

EXPERIMENTAL AND NUMERICAL AERODYNAMIC INVESTIGATION OF ADVANCED TAIL BOOM DESIGNS BASED ON OPTIMIZED THICK AIRFOIL PROFILES

Guillaume Legras, guillaume.legras@airbus.com, Airbus Helicopters SAS (France)

David Alfano, david.alfano@airbus.com, Airbus Helicopters SAS (France)

Abstract

The current paper aims at validating the aerodynamic performance of several advanced helicopter tail boom concepts answering to different aerodynamic optimization objectives. The flow solver validation has been carried out by comparing the numerical predictions with comprehensive measurement data obtained at the CNAM-IAT Wind Tunnel test facility. The comparison confirmed the accuracy and quality of the optimization results particularly in terms of ranking of the different optimal solutions. In this study, the database is further exploited to assess the capability of the CFD approach using the elsA solver to predict the aerodynamic characteristics of these optimized shapes.

Abbreviations

AH	Airbus Helicopters
AUSMP	Advection Upstream Splitting Method
CFD	Computational Fluid Dynamics
CNAM-IAT	Centre National des Arts et Métiers – Institut AéroTechnique
elsA	Ensemble logiciel de simulation Aérodynamique
NOTAR	NO Tail Rotor
RANS	Reynolds-Averaged Navier-Stokes
S-PIV	Stereoscopic Particle Image Velocimetry
SST	Shear Stress Transport
TB	Tail Boom
WTT	Wind Tunnel Test

Nomenclature

AoA	Angle Of Attack	[°]
c	Maximum depth/chord parallel to flow at 0° AoA of the model	[m]
C _x	Section vertical force coefficient in tail boom frame	[-]
C _y	Section side force coefficient in tail boom frame	[-]
C _p	Pressure coefficient (P-P _{ref})/q	[-]
h	Height of the model	[m]
P	Static pressure	[Pa]
P _{ref}	Reference Static pressure	[Pa]
q	Free stream dynamic pressure	[psf]

Re	Reynolds number, $\frac{\rho V_{wtt} c}{\mu}$	[-]
S	Reference surface, S=c*h	[m ²]
V _{wtt}	WTT velocity	[m/s]
y ⁺	Non-dimensional wall distance	[-]
ρ	Density	[kg/m ³]
μ	Absolute viscosity	[Pa.s]

1. INTRODUCTION

The main, mechanically driven, rotor of a classical helicopter transfers a reaction torque to the fuselage, which needs to be counterbalanced. The anti-torque demand is directly proportional to the main rotor required torque, which reaches the highest values in hover/low speed and high speed flight [1]. In those flight conditions, the flow features downstream the fuselage are complex, unsteady, characterized by strong interactions induced by the main rotor wake, with large variations in velocity magnitude and direction. The aerodynamic loads involved to trim the main rotor requiring complex design of dynamic parts, e.g. tail rotor, shrouded rotor like the Fenestron® and fixed parts, e.g. vertical stabilizers, bumper in order to handle the lateral stability and minimize the need in power.

Usually, the tail boom is more seen as a structural item, connecting the fuselage to the tail assembly and fairing the tail rotor drive shaft, than a dedicated aerodynamic component of the rotorcraft. In the literature, NASA's first investigated the aerodynamic loads prediction on

the tail boom. Wilson and Kelley [2][3] experimentally investigated the design characteristics of helicopter tail booms as well as the effects of protuberances (tail rotor drive-shaft cover, spoilers). They demonstrated the potential to reduce the rotor power consumed during hover, low speed and crosswind operating conditions by relieving the amount of tail rotor thrust and power required. Furthermore, Kelley et al. [4] pointed out that the non-linear force gradients near conditions of tail boom stall can also make precision yaw control more difficult for the pilot. Based on those observations, tail boom aerodynamic design should be oriented in order to minimize download and maximize its anti-torque contribution.

The tail boom contribution is driven by the pressure distribution over the cross-sectional shapes under the influence of the main rotor and the crosswind flows. Several studies intended to improve the tail boom effectiveness with respect to performance and handling qualities by passive control means using additional kits as strakes or spoilers [2][3][4][5][6], porous skin using various venting schemes [7] or active control means such as the NO Tail Rotor architecture [8].

Keeping these observations in mind, aerodynamic studies were performed in order to improve the effectiveness of tail boom thanks to dedicated optimized profiled shapes (patented by AH [6]). This approach gives more degrees of freedom, thus more potential gains, but should be done at an early helicopter design phase, rather than on improvement of existing designs using limited passive control means. Several innovative shapes were designed based on different aerodynamic objectives and constraints: symmetrical vs non symmetrical cross sectional tail boom shapes, hover download minimization vs. lateral force maximization for tail rotor relieve.

The current paper describes an intermediate maturity increase step of these advanced tail boom designs, thanks to an experimental investigation carried out at the CNAM-IAT WTT facility [9]. This procedure has permitted to build a comprehensive database (aerodynamic characteristics, pressure distribution and S-PIV measurements) in order to compare the various possible designs and improve the understanding of the aerodynamic behavior of thick profiles. The second objective of this study was to assess the capability of CFD, specifically the elsA solver developed by ONERA [10], to predict the aerodynamics of these optimized shapes. Results of the investigations are presented herein.

2. ADVANCED TAIL BOOM SHAPES DESIGNED USING OPTIMIZATION

The four investigated tail boom designs, illustrated in Figure 1, are the outcome of different targeted aerodynamic objectives.

The first one, **TB01**, corresponds to the tail boom concept of the US Army UH-1H utility helicopter tested by the NASA in the 80's [2][3]. This shape has been retained as a reference for crosschecks between WTT CNAM-IAT and NASA measurements. TB01 is built by extruding and scaling a single symmetrical 2D profile, roughly oval with large corner radii and without the tail rotor drive-shaft (see Wilson and Kelley for further details [2]).

The following three tail boom shapes, i.e. TB02, TB03 and TB04, have been designed by laying a 3D-surface respectively on three different families of 2D thick airfoils. Each family has been aerodynamically optimized by applying optimization algorithms to elsA simulations. All patented [6] designs are briefly described below:

- **TB02:** tail boom concept featuring 2D symmetric cross-sectional profiles aerodynamically optimized to maximize the lateral force; therefore, this concept contributes particularly to the anti-torque function, i.e. to relieve the tail rotor.
- **TB03:** tail boom concept featuring 2D symmetric cross-sectional profiles aerodynamically optimized to minimize the downforce (in hover and climb). Note that downforce reduction is obtained thanks to a reduction of profile width at the bottom or trailing edge region (flow directed from the top).
- **TB04:** tail boom concept featuring 2D non symmetrical cross-sectional profiles aerodynamically optimized for creating lateral forces as for TB02.

3. DESCRIPTION OF THE WIND TUNNEL TEST INVESTIGATION

3.1. Wind tunnel facilities

The WTT campaign has been performed in the CNAM-IAT facilities (Saint Cyr, France), mainly used for automotive and aeronautic applications. Tests have been conducted in the two wind tunnels:

- *S10 wind tunnel:* the test section is designed with slotted walls and ceiling to be insensitive to blocking effect. The test section dimensions are 5m x 3m x 10m.

The air-speed ranges from 0 to 55m/s, and the turbulence level is 0.5%.

- *S4 wind tunnel*: the key features are almost the same as S10 except that the maximum air-speed is 40m/s and the turbulence level is 1%.

A detailed description of the wind tunnels can be found in [10], whereas their sketches are provided in Figure 2.

3.2. WTT models

The design approach of the models and apparatus was inspired by the NASA campaigns [2]. The geometries investigated were down-scaled compared to equivalent tail booms implemented on a helicopter, mainly due to the dimension of the WTT facilities. The geometries principle is illustrated in Figure 3 and consisted of three different components made of composite material:

- The *first* and the *third* correspond respectively to root and tip-extensions, added to minimize 3D extremity effect on the area of interest.
- The *second* is the zone of interest, where each TB0x concept is implemented and instrumented.

Similarly to NASA's campaign [2] and for the first aerodynamic characteristic campaign, the models were positioned vertically and transversally to the incoming flow (see photographs of the installation of the model in the S10 facility Figure 3). A large end-plate was attached to the top segments to reduce 3D effects at tips, and to avoid contaminating the area of interest. A strut was extended through the floor to the mounting support, which allowed the mock-up to be rotated along its vertical axis in order to vary the flow incidence angle. A circular endplate was placed at root for the same reason as for the tip.

Concerning the S-PIV measurement campaign, the models laid horizontally on the side as shown in Figure 4. Thus, extremities end plates were replaced by structural interfaces. A rhodamine-based surface treatment was applied on the mock-up to reduce the spurious reflections of the laser sheet in the measurement region. Photographs of the installation of the model in the S4 facility are shown in Figure 4.

3.3. Test procedure and measurement accuracy

The experimental part of the study was divided into two main campaigns:

- The first one, performed in S10 wind tunnel, has been dedicated to measure the aerodynamics polars (global tail boom forces and moments) and the local pressure distributions.
- The second campaign conducted in the S4 wind tunnel, intended to characterize the down-stream flow field of TB02 and TB04 by implementing the S-PIV apparatus.

3.3.1 Aerodynamic polar measurements

This part of the campaign was conducted in the S10 wind tunnel. For the four geometries, databases were obtained that covered the ranges of Reynolds numbers Re as well as the angle of attack AoA seen by a typical full-scale helicopter's tail boom during hover and sideward flight operating conditions. Thus, data were obtained for three constant dynamic pressure values q (3, 20 and 39 psf). The selected incidence ranges depend on the symmetrical or non-symmetrical characteristic of the tail boom concept, in order to have some tests runs. For symmetrical concepts, TB01 to TB03, the incidence range is $[-20^\circ; +105^\circ]$ whereas for non-symmetrical configuration TB04 the range is $[-105^\circ; +105^\circ]$.

Notice that hereafter, two main flow incidences are identified:

- a) $AoA = -10^\circ$: incidence value roughly seen by the tail boom cross-sectional profiles during hover flight condition,
- b) $AoA = +90^\circ$: incidence value seen by tail boom cross-sectional profiles in lateral flight to the left (operating condition maximizing the tail rotor thrust for a helicopter with clockwise main rotor sense of rotation, seen from above).

All forces and moments are measured in the mock-up reference frame. In the current paper, data have been reduced to non-dimensional coefficient. The accuracies of the strain-gauge balance for vertical (C_x) and lateral force (C_y) coefficients are respectively $2 \cdot 10^{-3}$ and $6.5 \cdot 10^{-3}$. The sign convention for the incidence and the aerodynamic coefficients is given in Figure 6.

3.3.2 Static pressure measurements

Static pressure measuring ports were implemented on both TB02 and TB04 geometries. The pressure coefficient is defined as:

$$(2) \quad C_p = \frac{P - P_{ref}}{q}$$

With P the local static pressure, P_{ref} the static pressure measured on the lateral side of the WTT vein facility and q the dynamic pressure.

3.3.3 S-PIV measurements

Stereo Particle Image Velocimetry (S-PIV) campaign has been conducted in the S4 wind tunnel in order to assess the down-stream wake over selected geometries TB02 and TB04, both designed to optimize the lateral force but with different geometrical constraints. The flow incidences investigated are the two main one retained before: $AoA = -10^\circ$, resp. $+90^\circ$, corresponding to hover, resp. left lateral flow operating conditions.

The measurement window is located downstream the mock-up at mid-length of the study zone as shown in Figure 4. The S-PIV device is synchronized with 2 cameras of 4Mpixels in stereo configuration, thus measuring the 3 components of the particle velocity vector. The results are computed over a range of 400 images at 8Hz acquisition frequency.

3.4. Data validation

3.4.1 Confirmation of the non-influence of the model extremities on the study zone

Dedicated test runs were performed in order to ensure that there is no 3D effect induced by the extremities. To do so, wool tufts were implemented on both root and tip extremities of the TB01 model. Pictures of both zones are provided in Figure 5 and confirm that 2D flow is achieved on the region of interest, thus confirming the accuracy of the current approach.

3.4.2 Comparisons between WTT CNAM IAT and NASA measurements on TB01

In order to have a critical opinion of the WTT results obtained, a comparison with the NASA measurements of Wilson and Kelley [2] is proposed on the common configuration, i.e. tail boom concept TB01.

Figure 7 compares the NASA and our reference WTT measurements for different dynamic pressure values. Despite the fact that the facilities, the models (mainly endplate geometries) and apparatus are slightly different, the measurements prove to be relatively similar. Results of lateral

force in Figure 7a show similar gradients $\partial C_y / \partial AoA$ as well as same C_{ymax} occurring both at $AoA = \pm 10^\circ$ flow conditions, i.e. nearby hover flow condition. For AoA ranges characterized by strong flow detachments ($|AoA| > 10-12^\circ$), differences appear between both campaigns. The comparison in terms of C_x characteristics, shown in Figure 7b, indicates that the current campaign predicts lower value than the NASA one. The main explanations herein might come from the endplates geometrical difference as well as the model roughness (the current might be smoother than the NASA one) and the WT turbulence intensities. However, based on these observations it is concluded that the current campaign measurements are coherent and exploitable.

3.4.3 Influence of the Reynolds number on TB01

Due to the sensitivity of thick profiles to Reynolds numbers Re and the high range of Re values experienced by tail boom on the helicopter, it is proposed to briefly analyze its effect on the polar characteristics of TB01 shape.

The Figure 7 presents the influence of the Reynolds number on the aerodynamic coefficients of the TB01 concept, through variation of the dynamic pressure. For very low Reynolds numbers ($q = 3\text{psf}$), the polar suggests a stall of the profile nearby $AoA = \pm 10^\circ$. On the contrary, for higher Reynolds number ($q \geq 25\text{psf}$), the aerodynamic polars are closer to each other characterized by symmetrical feature and a stall occurrence delayed to $12/14^\circ$. In operating conditions, for which the tail boom is highly loaded (hover and crosswind), it might be expected that the cross sectional flow is super-critical resulting in higher stability range regarding stall since the boundary layer is turbulent. As a consequence, only the results for the dynamic pressure $q = 39\text{psf}$ are retained for the next analysis.

4. DESCRIPTION OF THE NUMERICAL MODELS

4.1. Configurations modeled and meshing strategy

In order to be as comparable as possible to the experimental data, it was decided to numerically model the four tail boom concepts in the S10 wind tunnel experimental environment. To facilitate the model set-up, a Chimera assembly approach has been considered, composed of two main components meshed separately: the wind tunnel

facility mesh and the tail boom mesh embedded in the previous one. The Chimera approach allows to easily substitute the tail boom model and, for a given model, to change its incidence by simply rotating the tail boom mesh in the wind tunnel one. A further advantage is that the wind tunnel mesh is independent of the tail boom meshes and their setting angles.

Both wind tunnel and tail boom geometries have been meshed, by means of the commercial grid generator Ansys ICFM-CFD, using a multi-block structured approach. The cells adjacent to the wall surfaces of the tail boom mesh have been set to ensure a dimensionless wall-distance between $0.1 < y^+ < 3$. For the mock-up root and the S10 vein walls, a wall law is imposed so that the mesh constraints are released. The S10 wind tunnel vein is meshed using 9.8 million grid points whereas the tail boom mesh models count 5.7 million grid points. Figure 8 presents a detailed view of the TB01 concept in S10 wind tunnel mesh model.

4.2. Numerical methods

All numerical simulations are carried out using the elsA CFD software developed at ONERA [11]. The code solves the Favre-Reynolds-averaged Navier-Stokes equations on multi-block structured meshes using a cell-centered finite-volume approach. It also allows the use of the Chimera method dedicated to model complex geometries assembly (examples of elsA applications over helicopter can be seen in references [12][13]).

Computations discussed here were run using a steady state approach. Although a real steady state can hardly be achieved in wakes of very thick airfoils, this simple approach still allows working on shape first-order understanding. The spatial discretization is based on a finite-volume discretization of the equations written in conservative form. The viscous fluxes are resolved thanks to a centered scheme whereas inviscid fluxes are computed using the Advection Upstream Splitting Method Preconditioned (AUSMP) [14] in order to better predict low Mach number flow. The time-marching is performed by an efficient implicit time integration scheme based on the backward Euler scheme and a scalar lower-upper (LU) symmetric successive over relaxation (SSOR) method. Turbulence is modeled by the transport two-equation $k-\omega$ model with Shear Stress Transport (SST) [16] proposed by Menter [15]. As explained before, the flow is assumed to be fully turbulent. Concerning Chimera technique parameters, the Alternative Digital Tree (ADT) preconditioning-based technique has been used to determine donor

cells. Masking of the tail boom mock-up in the S10 wind mesh models has been achieved by the Meakin X-ray technique. Second-order Chimera interpolations have been used to transfer the solution between the overlapping grids. A total of 10'000 iterations have been required to ensure an acceptable convergence level.

5. RESULTS AND DISCUSSION

Results and comparison of experimental and numerical approaches are presented hereafter. As announced in the introduction, the main objective of this comparison is to confirm the ranking of the concepts and the validity of the optimization methodology, as well as to validate the numerical approach.

5.1. Aerodynamic characteristics

Figure 9 compares the aerodynamic characteristics of the three advanced tail boom concepts TB02, TB03 and TB04. Experimental and numerical polars obtained for $q=39\text{psf}$ are plotted. Based on the sign convention of Figure 6, a reduction of the coefficient C_x at $AoA=-10^\circ$ means a reduction of the tail boom download in hover, whereas maximizing the left lateral force in hover conditions (for clockwise rotor) reflects in high negative magnitude of lateral coefficient C_y .

Experimental results show that the ranking of the tail boom concepts in terms of vertical and lateral force in hover is as expected. TB03, designed to minimize vertical force using symmetrical profiles, proves to have the lowest C_x over the linear stable part of the polar compared to the other tail boom concepts (approximately twice lower than TB02 at $AoA=0^\circ$). TB02, designed to maximize the lateral force with a symmetrical profile clearly improves both the gradient $\partial C_y / \partial AoA$ and $C_{y\text{max}}$ value by a factor nearly two, compared to TB03. At the same time, range of stable incidence has slightly increased. TB04, optimized for lateral force in hover by means of non-symmetrical profiles, shows interesting features:

- the C_x vs. AoA variation in the linear region is roughly similar to the symmetrical TB02 concept;
- for $AoA=-10^\circ$, the lateral force coefficient C_y is nearby twice that of TB03 and 30% greater than for TB02, proving the efficiency of the concept.

However, TB04 differs mainly from TB02 by the shift in incidence (i.e. AoA for $C_y=0$) due to the non-symmetrical shape. The main consequence expected is that during a transition maneuver from hover to left lateral flight (i.e. AoA

increasing) TB04 will relieve more the tail rotor thrust (or provide greater contribution on anti-torque) than TB02 and TB03. Compared to TB02, the other interesting observation is that the C_y magnitude transition from the linear to the high incidence part is reduced, suggesting that pilot maneuver from hover to left lateral flight will be also relatively smoother. To resume, the WTT data validates the optimization methodology since the ranking expected has been demonstrated. Furthermore TB04 proves to be very promising, and shows the potential of a non-symmetrical tail boom design compared to a symmetrical one.

Figure 9 allows comparing both experimental measurements (symbols) and CFD elsA predictions (lines). The numerical approach proves to be in very good agreement with experiment, in particular on the prediction of the previous tail boom ranking, as well as the quantitative figures of lateral coefficient C_y (gradient in the linear part, the $C_{y\max}$ magnitude with corresponding incidence). However, the simulations tend to over-estimate the coefficient C_x over the three configurations without modifying the conclusions. The authors want to remind the reader that the numerical results presented herein at high incidence, where flow separation occurs, are strongly unsteady. Past experience showed that numerical results from a RANS approach indeed differ from time-averaged equivalent URANS ones, which might explain the coherent shift particularly in the C_x coefficient for all tail boom concepts. Nevertheless, the difference between RANS and URANS results is not expected to be large enough to change the ranking.

Figure 10 presents the distributions of the pressure coefficient C_p at mid-height cross section of TB02 and TB04 models. Plots are provided in cylindrical coordinates with respect to the center of the profile at mid-height. Both experimental (filled symbols) and numerical (empty symbols) results for two operating conditions are shown. At first, Figure 10a compares plots for $AoA=-10^\circ$. The numerical results prove to be very similar to the measurements. The C_p negative peak, where flow is accelerated over the corner facing the incoming flow, thus contributing to the lateral force, is correctly captured in terms of both position and amplitude. The C_p deficit proves to be greater for TB04 in coherence with the results shown in Figure 9. Both experimental and numerical results highlight a second flow acceleration nearby the azimuthal position $320\pm 20^\circ$, more pronounced for TB04.

Figure 10b illustrates results for $AoA=+90^\circ$ corresponding to left lateral flight condition. Note that even if TB02 and TB04 are geometrically different, their aerodynamic performance proves to be very similar for this particular flow condition. Results also highlight that the numerical approach correctly predicts the C_p distribution: in particular the two negative C_p peaks located at the two corners facing the upstream flow, as well as the C_p magnitude applied on the opposite face of the concepts are well captured.

Previous observations lend support that numerical CFD approach is capable to correctly predict both global efforts and local aerodynamic features.

5.2. Qualitative analysis of the S-PIV measurements

This section is dedicated to a brief analysis of the S-PIV measurements in a plane located at mid-height, downstream the tail boom concepts, thus focusing on the wake. The measurements available are the three velocity components, their time-averaged and unsteady fluctuation values. In the present section, just a qualitative analysis is proposed.

Figure 11 presents the time-averaged magnitude of the longitudinal velocity downstream the TB02 and TB04 for $AoA=-10^\circ$ (i.e. hover condition). The downstream wake can be clearly observed through the velocity deficit (region in blue). The characteristic of the wake is a good indicator of the download behavior for the $AoA\approx-10^\circ$. The TB04 configuration, which only differs from TB02 by its non-symmetrical design features, proves to greatly reduce the downstream wake extension compared to TB02. This observation further confirms the better performance in left lateral operating conditions of the TB04 previously observed on both aerodynamic characteristics (Figure 9) and pressure distributions (Figure 10).

6. CONCLUSIONS

This paper has presented an aerodynamic investigation of three advanced tail boom designs. Each concept has been designed based on thick airfoil profiles optimized for different objectives (e.g. hover downwash minimization, hover lateral force maximization in order to relieve tail rotor) and geometrical constraints (e.g. possibility to manufacture those shapes at affordable costs, structural strength, etc.). The purpose of the investigation was to confirm the aerodynamic characteristics and concept rankings and validate the numerical capability to predict both the ranking and quantitative values. To do so, an

experimental campaign was conducted at the CNAM-IAT facility in order to build a comprehensive database. The experimental procedure was first validated by crosschecking the CNAM-IAT measurements with past NASA wind tunnel ones [2] (on same reference shape based on the US Army cross sectional shape). Then, the advanced concepts were compared in terms of aerodynamic polars over a range of flow incidence that encompasses the flow condition seen by a full scale helicopter. The experimental results clearly confirmed the expected design ranking. Analysis of the local measurements (pressure distributions and S-PIV) further confirmed the previous observations and helped to further understand the basic aerodynamic behavior of those different advanced tail boom concepts.

The second main objective of this paper was to validate the numerical CFD approach using the elsA solver of ONERA. The comparison with the current wind tunnel database clearly confirms the capability of the numerical approach to predict the aerodynamic characteristics (thus the design ranking) as well as local quantities.

Finally the current methodology proves its potential to improve tail boom designs, as well as their impact on helicopter global performance.

7. FUTURE PERSPECTIVES

A non-symmetric Tail boom, derived from the TB04 concept, is present on the RACER Technology Demonstrator. The RACER Technology Demonstrator (see Figure 12) new formula, done in the EU H2020 / Clean Sky 2 Program framework, will be investigated in a comprehensive new formula exploration flight test campaign. This flight tests campaign will allow a step forward in non-symmetric tail-boom assessment, in a relevant flight environment.

8. ACKNOWLEDGMENTS

The authors are grateful for the support from the CNAM-IAT Institute members, particularly Enrico Bergamini, Patrick Fournier and Francesco Grasso.

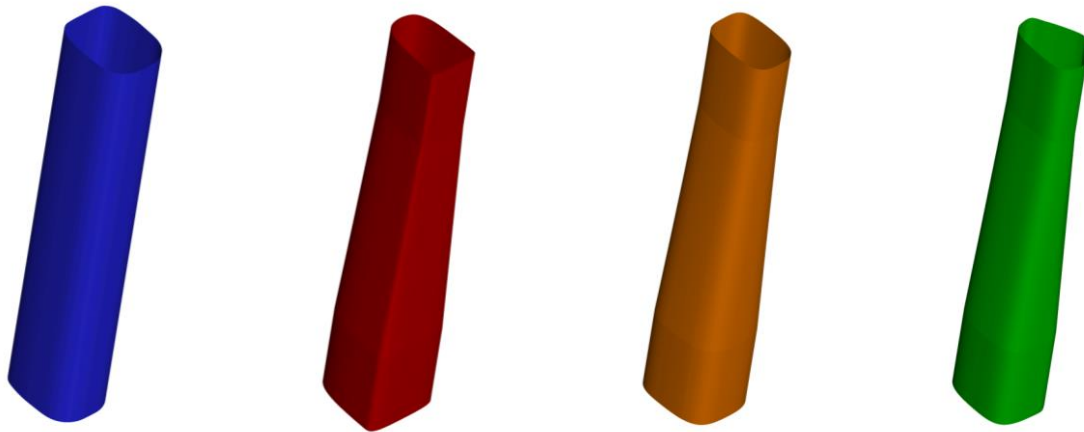
Part of this work has received funding from the European Union's Horizon 2020 Research and Innovation program under Grant Agreements No CS2-FRC-2014-2015 and subsequent amendments. The Clean Sky Joint Undertaking Team is dully acknowledged for continuous support in Implementation.

9. REFERENCES

- [1] J. G. Leishman, "Principle of Helicopter Aerodynamics", Cambridge Aerospace Series.
- [2] J. C. Wilson and H. L. Kelley, "Aerodynamic Characteristics of Several Current Helicopter Tail Boom Cross Sections Including the Effect of Spoilers", NASA Technical Paper 2506, 1986.
- [3] H. L. Kelley, C. A. Crowell and John C. Wilson, "Two-Dimensional Aerodynamic Characteristics of Several Polygon-Shaped Cross-Sectional Models Applicable to Helicopter Fuselages", NASA Technical Paper 3223 / AVSCOM Technical Report 92-B-002, 1992.
- [4] H. L. Kelley, C. A. Crowell, K. R. Yenni and M. B. Lance, "Flight Investigation of the Effect of Tail Boom Strakes on Helicopter Directional Control", NASA Technical Paper 3278 / ATCOM Technical Report 93-A-003, 1993.
- [5] C.A. Crowell and H. L. Kelley, "Aerodynamic Effect of Strakes on Two-Dimensional Tail Boom Models of the OH-58A and the OH-58D Helicopters", NASA TM-4248, AVSCOM TR-90-B-010, 1990.
- [6] R. A. Lockwood, W. A. Kelly and R. W. Cason, "Flight Characteristics Test of the UH-60A With Tail Boom Mounted Strake". USAAEFA Proj. No. 85-07, U.S. Army, Oct. 1986.
- [7] D. W. Banks, H.L. Kelley, "Exploratory Investigation of Aerodynamic Characteristics of Helicopter Tail Boom Cross-Section Models with Passive Venting, NASA TP-2000-210083, June 2000.
- [8] E. P. Sampatacos, K. M. Morger, and A. H. Logan, "NOTAR—The Viable Alternative to a Tail Rotor", AIAA-83-2527, 1983.
- [9] D. Alfano, G. Legras, D. Leusink, "Method of Optimizing Sections of a Tail Boom for A Rotary Wing Aircraft", US Patent n° US2018029702, 2018.
- [10] CNAM-IAT website, <http://www.iat.cnam.fr/>
- [11] L. Cambier, S. Heib and S. Plot, "The Onera elsA CFD Software: Input From Research and Feedback From Industry, Mechanics & Industry", Vol. 14, No. 3, 2013, pp. 159-174, doi:10.1051/meca/2013056.
- [12] T. Renaud, M. Costes, S. Péron, "Computation of GOAHEAD configuration with Chimera assembly", Aerospace Science and Technology, 19(1):50–57, 2012
- [13] D. Desvigne and D. Alfano, "Rotor-Head/Fuselage Interactional Effects on Helicopter Drag: Influence on the Complexification of the Rotor-Head

Geometry”, proceedings of the European Rotorcraft Forum, 2013.

- [14] M.-S. Liou and J.-R. Edwards. "AUSM schemes and extensions for low Mach and multiphase Flows", 30th Computational Fluid Dynamics, 1999-03 Von Karman lecture series, 1999.
- [15] F. R. Menter, "Improved Two Equation k- ω Turbulence Models for Aerodynamic Flows", Technical Report NASA Technical Memorandum 103975(1992).
- [16] F. R. Menter, "Zonal Two Equation k- ω Turbulence Models for Aerodynamic Flows", AIAA paper 93-2906 Proceedings of the 24th Fluid Dynamics Conference, 1993.
- [17] R. T. Meakin, "Object X-Rays for Cutting Holes in Composite Overset Structured Grids", 15th AIAA Computational Fluid Dynamics Conference, 2000.



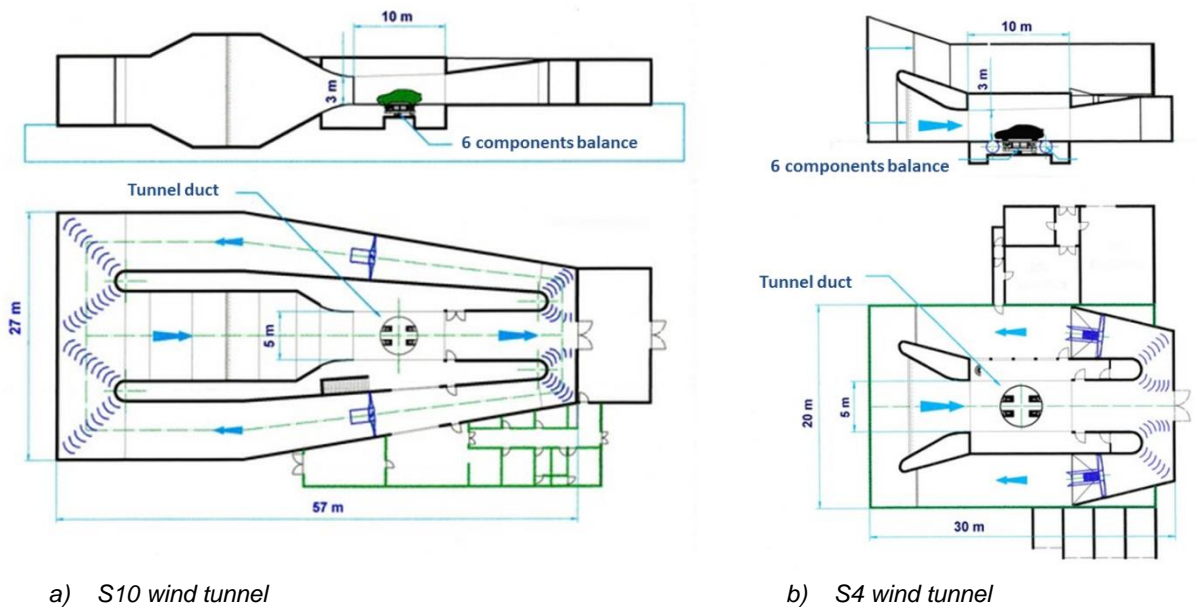
a) TB01

b) TB02

c) TB03

d) TB04

Figure 1 Views of the tail-boom concepts



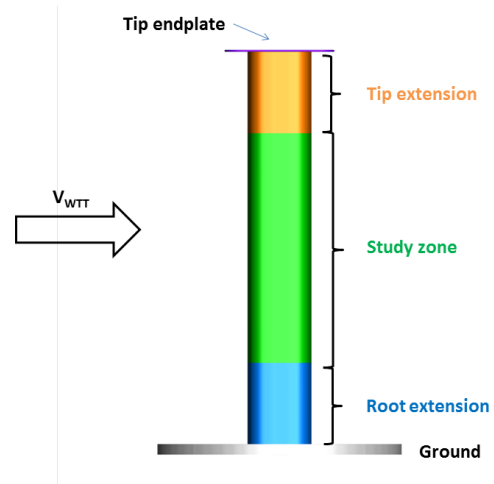
a) S10 wind tunnel

b) S4 wind tunnel

Figure 2: CNAM–IAT WTT wind tunnels [10]

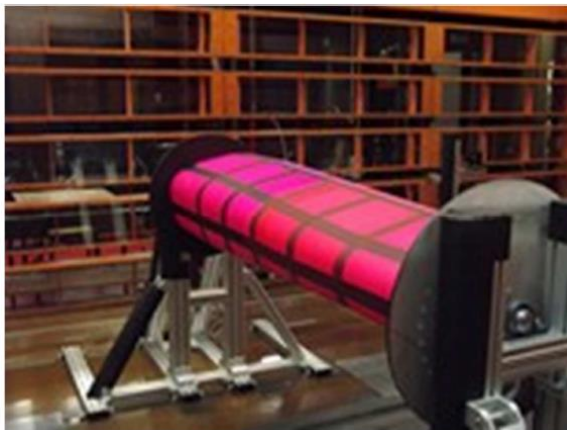


a) Photo of the TB01 mock up in CNAM-IAT S10 Wind Tunnel

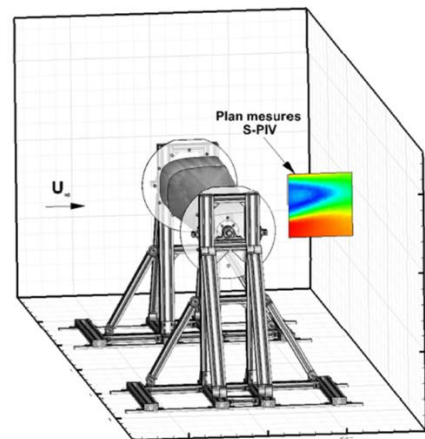


b) Scheme of the basic principle of the tail boom mock up

Figure 3 Scheme (up) and photos (bottom) of the tail-boom mock-up in CNAM-IAT facility.

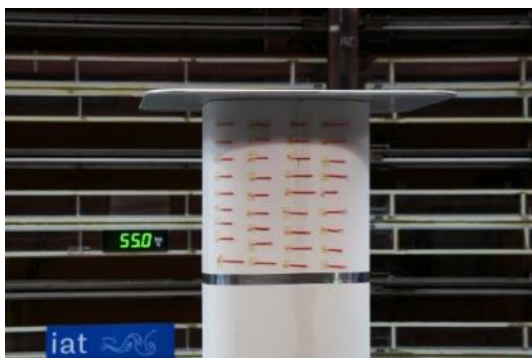


a) Photography of TB02 in S4 wind tunnel

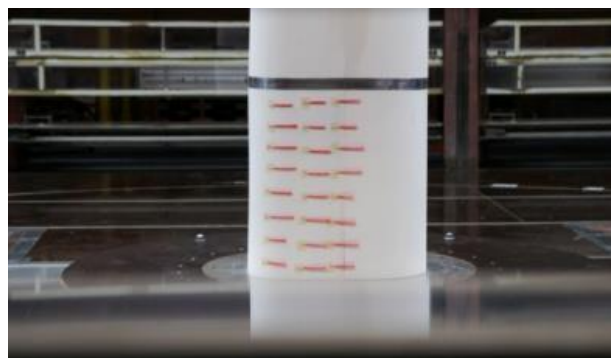


b) S-PIV architecture

Figure 4 TB02 S-PIV measurements in CNAM-IAT S4 wind Tunnel



a) Tip extremity



b) Root extremity

Figure 5 Photos of the wool tuft at TB01 mock-up extremities $q = 39 \text{ psf}$ and $\text{AoA} = 0^\circ$

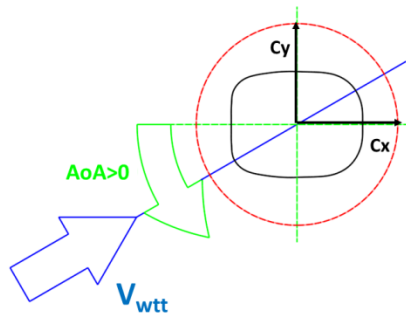
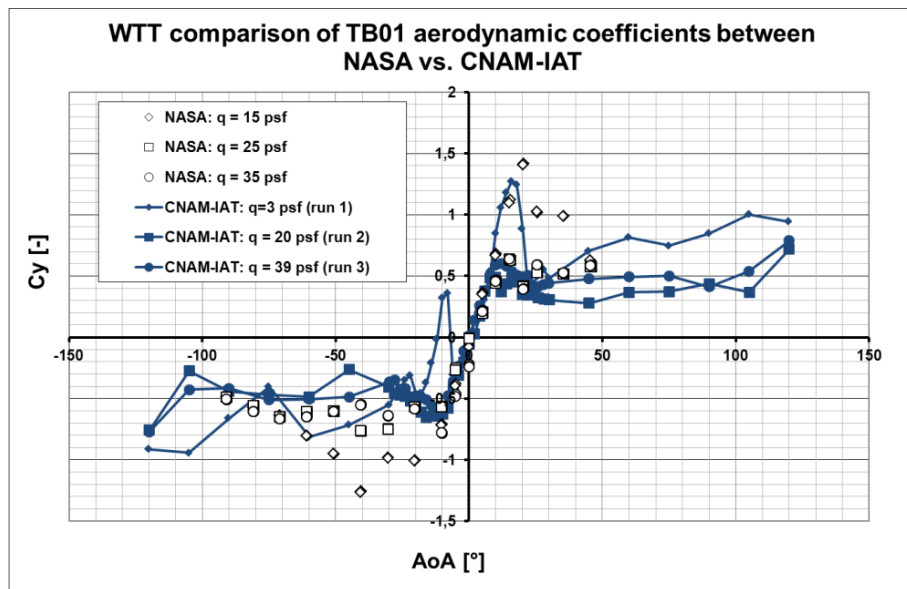
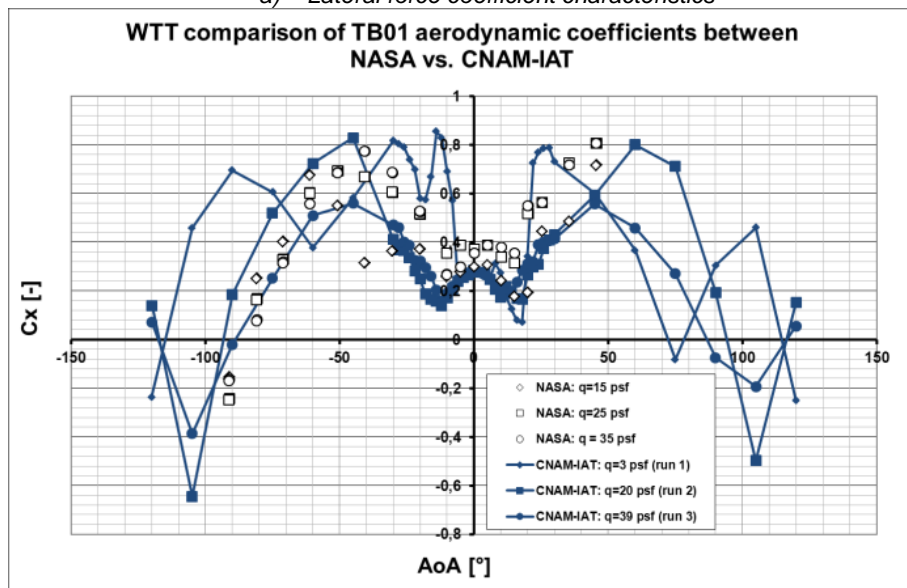


Figure 6: Sign convention of the flow incidence and aerodynamic coefficients other TB01.



a) Lateral force coefficient characteristics



b) Vertical coefficient characteristics

Figure 7 Comparison of TB01 aerodynamic coefficients (tail boom frame) between NASA WTT measurement [2] and current WT campaign at CNAM-IAT.

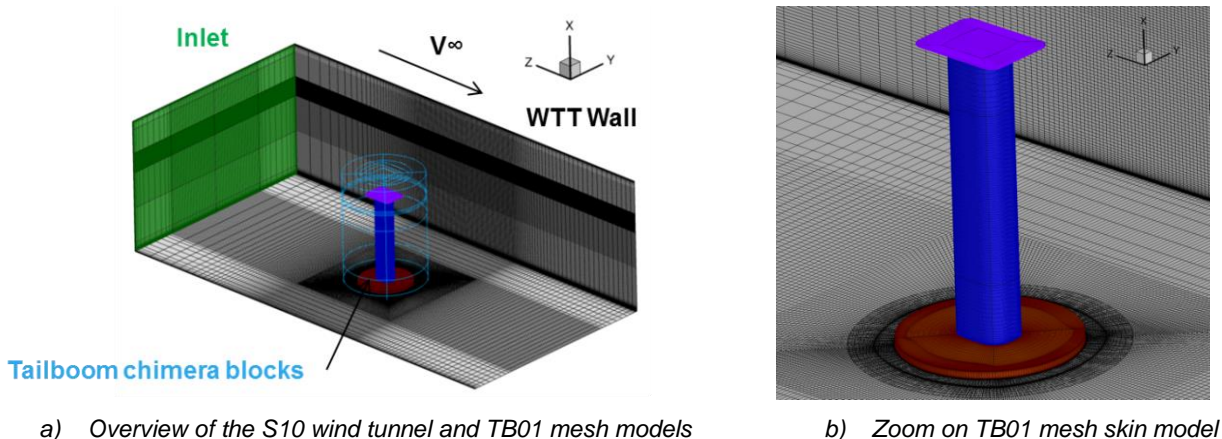
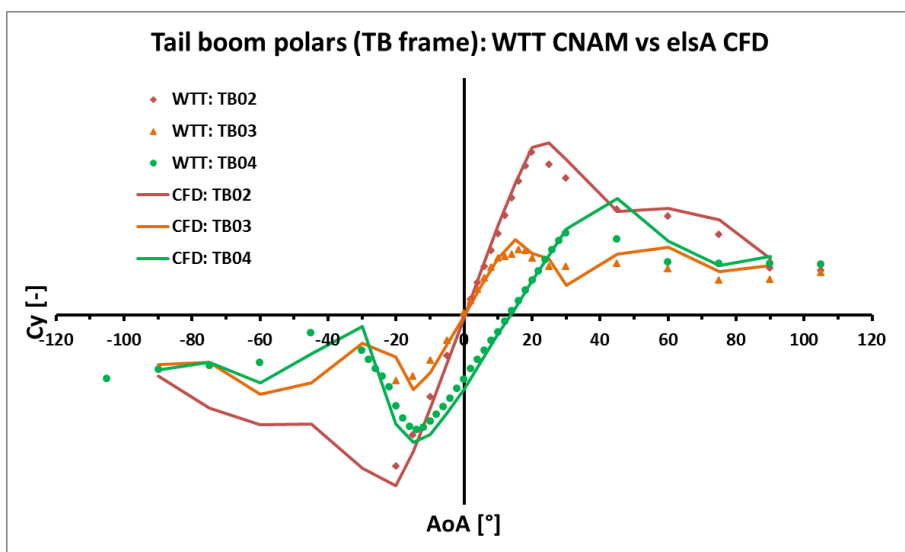
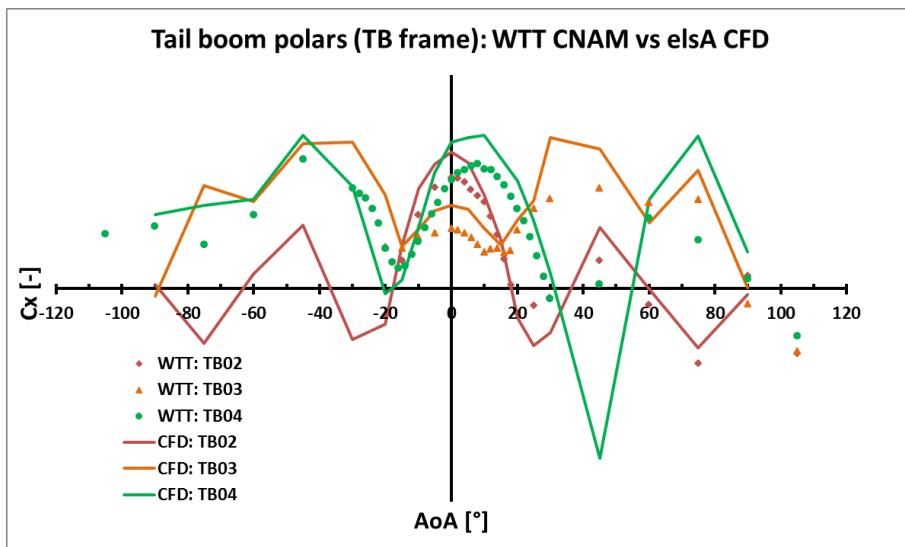


Figure 8. 3D views of the TB01 mock-up and S1 facility mesh models

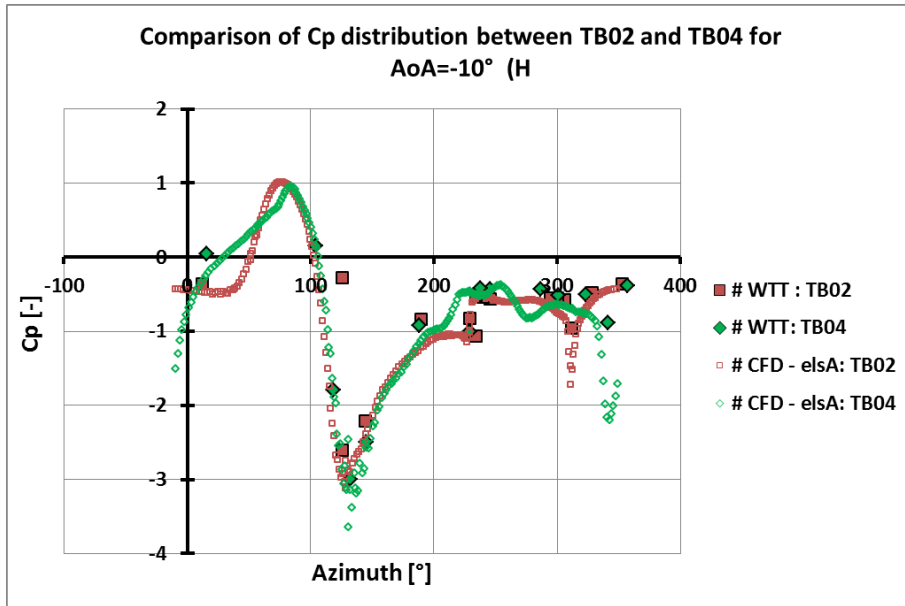


a) Lateral force coefficient characteristics

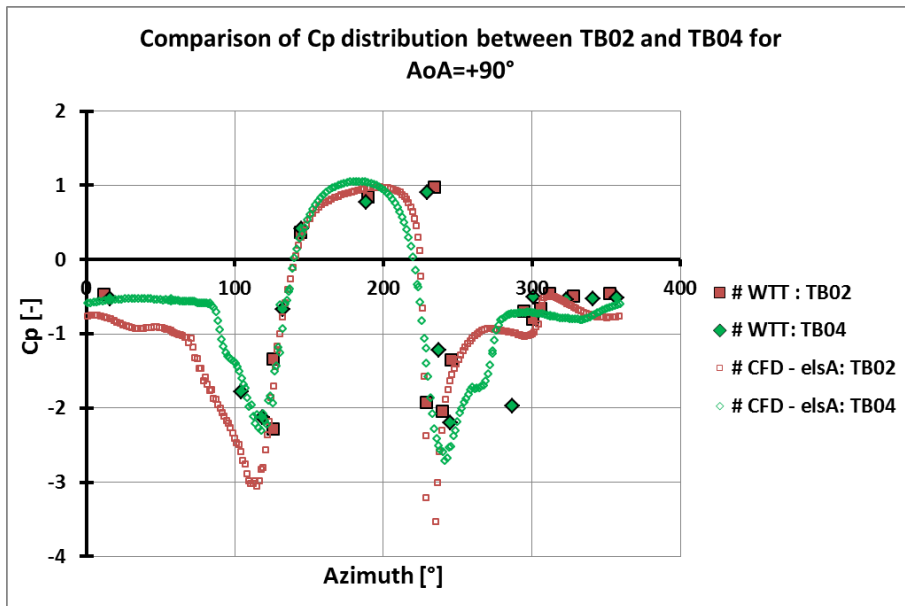


b) Vertical coefficients characteristics

Figure 9 Comparison between WTT and CFD elsA results of the aerodynamics coefficients (tail boom frame) of several tail boom concepts



a) *Cp* distribution for $AoA=-10^\circ$



b) *Cp* pressure distribution

Figure 10 Comparison between WTT and CFD elsA results of the *Cp* pressure coefficients of TB02 and TB04 concepts

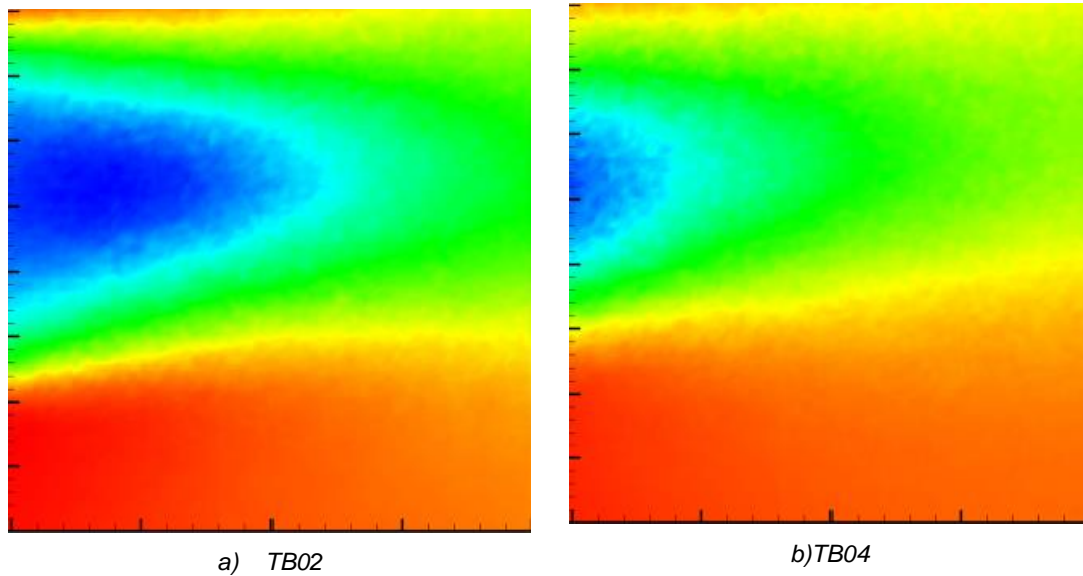


Figure 11 Comparison between TB02 and TB04 concepts of S-PIV measurements of downstream time-averaged longitudinal velocity magnitude (level color from blue (negative value) to red meaning increasing velocity magnitude) for $AoA=-10^\circ$



Figure 12 Press release of the RACER High Speed Helicopter Technology Demonstrator, developed in the frame of EU H2020 / Cleansky 2 Program